# Semiclassical control theory of coherent anti-Stokes Raman scattering maximizing vibrational coherence for remote detection

J. Chathanathil, G. Liu, and S. A. Malinovskaya

*Department of Physics, Stevens Institute of Technology, Hoboken, New Jersey 07030, USA*

A semiclassical theory that describes the generation of a coherent anti-Stokes Raman scattering (CARS) signal is presented that maximizes vibrational coherence in a mode predetermined by the pump, the Stokes, and the probe chirped pulse trains and takes into account the field propagation effects in a cloud of molecules. The buildup of the anti-Stokes signal, which may be used as a molecular signature in the backward CARS signal, is demonstrated numerically. The theory is based on the solution of the coupled Maxwell's and Liouville–von Neumann equations and focuses on the quantum effects induced in the target molecules by the control pulse trains. A deep convolutional neural network technique is implemented to evaluate time-dependent phase characteristics of the control fields. The effect of decoherence induced by spontaneous decay and collisional dephasing is examined.

## I. INTRODUCTION

Coherent anti-Stokes Raman scattering (CARS) belongs to the frontiers of nonlinear optics methods suited for imaging, sensing, and detection without labeling or destruction [1]. The implementation of ultrafast pulses in stimulated Raman spectroscopy in general and CARS in particular brings the advantages of high peak power, three-dimensional spatial resolution, and femtosecond time resolution to monitor vibrational dynamics [2–12]. Femtosecond CARS has been widely used and nowadays advances toward solving tasks related to single-molecule spectroscopy, molecular-specific imaging, sensing traces of molecules, and remote detection [13–18]. Success in these areas depends on a high level of chemical sensitivity and specificity, the signal-to-noise ratio, and the CARS signal intensity. Because the Raman fields' evolution is proportional to the macroscopic induced polarization [19], which in its turn is proportional to a microscopic quantum property of the material, quantum coherence, crafting ultrafast laser pulses to generate the maximum coherence in the target molecules lies at the root of any method to impact the molecular-specific response and to significantly enhance the signal. To date, there have been a number of methods developed to achieve the maximum coherence leading to the enhancement of the signal from predetermined vibrational modes in CARS using shaped ultrafast pulses. Among pioneering works, including those for remote detection, are Refs. [20–32] proposing different phase shapings of the ultrafast pulses. Other notable works involve multiplex CARS using a combination of a narrow-band chirped pump and probe and a transform-limited broadband Stokes pulse [33] and a proposal of double parabolic phase functions in stimulated Raman scattering (SRS) [34].

In this paper, we present a semiclassical theory of the generation of an anti-Stokes signal by creating the maximum vibrational coherence in a predetermined mode with the pump, the Stokes, and the probe chirped pulse trains in the four-wave mixing in CARS and take into account the field propagation effect in a cloud of molecules. The motivation is to demonstrate the buildup of the anti-Stokes signal, which may be used as a molecular signature in the backward CARS signal. The theory is based on the solution of coupled sets of Maxwell's and Liouville–von Neumann equations and focuses on the quantum effects induced in the target molecules by the shaped laser pulse trains. We analyze the enhancement of the backscattered anti-Stokes signal upon multiple scattering of radiation from the target molecules, which modifies propagating fields. We examine the impact of decoherence induced by spontaneous decay and collisional dephasing. We demonstrate that decoherence due to spontaneous decay can be mitigated by applying the control pulse trains with the train period close to the decay time.

This study demonstrates the buildup of coherent anti-Stokes signal as a result of controllability of the vibrational coherence in the target molecules upon the propagation of four chirped pulse trains subject to multiple-scattering events, utilizes the pulse train properties to mitigate decoherence, and implements the deep convolution network approach to evaluate the phase of the propagating fields, which provides us with information about the relative phase change between the pump, the Stokes, the probe, and the anti-Stokes pulses.

As a case study we use methanol vapor. Methanol molecules have Raman active symmetric 2837-$cm^{-1}$ (85.05 THz) and asymmetric 2942-$cm^{-1}$ (88.20 THz) stretch modes. These values are within the range of molecular group vibrations in various biochemical species, which span from 2800 to 3100 $cm^{-1}$, making methanol a suitable choice as a surrogate molecule for nonhazardous experiments in the laboratory. Thus the results of methanol studies would be useful for the development of remote detection schemes as well as for environmental analyses.
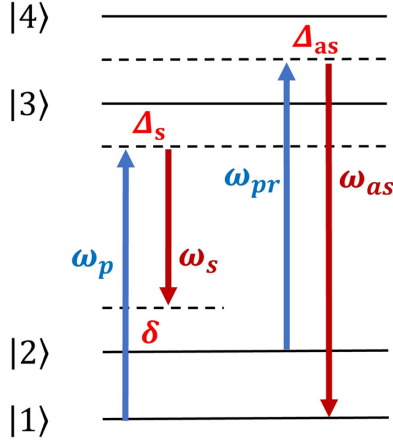
FIG. 1. Schematic of CARS: the pump ($\omega_p$) and the Stokes ($\omega_s$) fields interact with the ground vibrational state $|1\rangle$ and the excited vibrational $|2\rangle$ state of the ground electronic state in the target molecule to create a superposition state with coherence $\rho_{12}$. The probe ($\omega_{pr}$) field interacts with this superposition state to generate an anti-Stokes field at frequency $\omega_{as}$. Parameters $\Delta_s$ and $\Delta_{as}$ are the one-photon detunings, and $\delta$ is the two-photon detuning.

Various setups are available to perform CARS experiments satisfying the phase-matching conditions to separate the directional anti-Stokes signal from the incident fields. However, for particles having a size comparable to the wavelength, the phase-mismatched factor is small, and it was shown that the non-phase-matched CARS can provide an effective method to probe complex molecules [22,35]. For methanol, the ratio $4\pi\rho_0/\lambda \ll 1$, where $\rho_0 \sim 10^{-10}$ m is the target molecule diameter; this relaxes the phase-matching condition and permits consideration of the collinear copropagating fields' configuration.

The paper is organized as follows. In Sec. II, a theoretical framework is formulated. Section III discusses the machine learning approach for a numerical analysis of the phase of the propagating fields. Section IV contains the numerical results

for methanol and a discussion. The paper concludes with a summary.

## II. THEORETICAL FRAMEWORK

### A. Coupled Maxwell's and Liouville–von Neumann formalism

CARS is a third-order nonlinear process in which three beams, the pump, the Stokes, and the probe, at frequencies $\omega_p$, $\omega_s$, and $\omega_{pr}$, respectively, interact with the electronic vibrational—vibronic—states of the target molecules to generate the anti-Stokes field at frequency $\omega_{as} = \omega_p + \omega_{pr} - \omega_s$ (Fig. 1). In our control scheme, we use linearly chirped pulse trains which read

$$
E_i(t) = \sum_{k=0}^{N-1} E_{i0} \exp\left\{ -\frac{(t - t_c - kT)^2}{2\tau^2} \right\}
$$
$$
\times \cos\left\{ \omega_{i0}(t - t_c - kT) + \alpha_i \frac{(t - t_c - kT)^2}{2} \right\}.
\tag{1}
$$

Here, $T$ is the pulse train period, $t_c$ is the central time when the peak value of the Gaussian field envelope is $E_0$, $\tau$ is the chirp-dependent pulse duration, $\omega_{i0}$ is the carrier frequency, and $\alpha_i$, $i = p, s, pr$, is the linear chirp rate of an individual pump, Stokes, or probe pulse in the respective pulse train. The values of $\alpha_i$ are chosen in accordance with the control scheme, which implies $\alpha_s = -\alpha_p$ and $\alpha_{pr} = \alpha_s - \alpha_p$ for $t \leqslant t_c$; and $\alpha_s = \alpha_p$ and $\alpha_{pr} = 0$ for $t > t_c$ [36]. Such chirped pulses induce the maximum coherence between vibronic states in the target molecules via adiabatic passage provided the two-photon detuning $\delta = 0$. Any slightly different vibrational mode not satisfying the two-photon resonance condition, $\delta \neq 0$, is suppressed. The selectivity of the mode excitation is determined by the condition $\tau\delta \geqslant 1$. The chirped pulse duration $\tau$ relates to the transform-limited pulse duration $\tau_0$ as $\tau = \tau_0(1 + \alpha'^2/\tau_0^4)^{1/2}$, and the temporal ($\alpha$) and spectral ($\alpha'$) chirps relate as $\alpha = \alpha'\tau_0^{-4}/(1 + \alpha'^2/\tau_0^4)$.

The matrix Hamiltonian written in the interaction representation and in the rotating-wave approximation (RWA) reads

$$
H = \frac{\hbar}{2}
\begin{pmatrix}
0 & 0 & \Omega_{p_0}(t)e^{i\Delta_s t + i\frac{\alpha_p}{2}t^2} & \Omega_{as_0}(t)e^{i\Delta_{as}t} \\
0 & 0 & \Omega_{s_0}(t)e^{i\Delta_s t + i\frac{\alpha_s}{2}t^2} & \Omega_{pr_0}(t)e^{i\Delta_{as}t + i\frac{\alpha_{pr}}{2}t^2} \\
\Omega_{p_0}^*(t)e^{-i\Delta_s t - i\frac{\alpha_p}{2}t^2} & \Omega_{s_0}^*(t)e^{-i\Delta_s t - i\frac{\alpha_s}{2}t^2} & 0 & 0 \\
\Omega_{as_0}^*(t)e^{-i\Delta_{as}t} & \Omega_{pr_0}^*(t)e^{-i\Delta_{as}t - i\frac{\alpha_{pr}}{2}t^2} & 0 & 0
\end{pmatrix}.
\tag{2}
$$

Here, $\Omega_{p_0}(t) = -\mu_{31}/\hbar E_{p_0}(t)$, $\Omega_{s_0}(t) = -\mu_{32}/\hbar E_{s_0}(t)$, $\Omega_{pr_0}(t) = -\mu_{42}/\hbar E_{pr_0}(t)$, and $\Omega_{as_0}(t) = -\mu_{41}/\hbar E_{as_0}(t)$ are the Rabi frequencies of respective fields, $\mu_{ij}$ is a dipole moment, $\Delta_s$ and $\Delta_{as}$ are the one-photon detunings on transitions $|1\rangle \rightarrow |3\rangle$ and $|1\rangle \rightarrow |4\rangle$, respectively.

To account for the propagation effects in the scattering process, we combine the Liouville–von Neumann equation for the states with Maxwell's equations for the fields. The displacement current is determined as $D = \epsilon_0 E + P$, where $P$ is the expectation value of the induced dipole moment and $\epsilon_0$ is the permittivity of free space. The effects arising from

magnetization are neglected giving $B = \mu_0 H$, where $\mu_0$ is the permeability of free space. The wave equation for a field propagating in the $\hat{z}$ direction and having polarization in the $XY$ plane reads

$$
\left( \frac{\partial}{\partial z} + \frac{1}{c}\frac{\partial}{\partial t} \right)\left( -\frac{\partial}{\partial z} + \frac{1}{c}\frac{\partial}{\partial t} \right)E = -\mu_0 \frac{\partial^2 P}{\partial t^2}.
\tag{3}
$$

Assuming the field is $E(z, t) = \frac{1}{2}[E_0(z, t)e^{-i[\omega t - kz - \phi(z,t)]} + $ c.c.] and considering $E_0(z, t)$ and $\phi(z, t)$ as slowly varying

functions of position and time, Eq. (3) can be written as

$$-2k\left(\frac{\partial E_0(z,t)}{\partial z} + \frac{1}{c}\frac{\partial E_0(z,t)}{\partial t}\right)\sin\left[\omega t - kz - \phi(z,t)\right]$$

$$= -\mu_0\frac{\partial^2}{\partial t^2}P(z,t). \tag{4}$$

Substituting $P(z,t) = \frac{1}{2}[P_0(z,t)e^{-i[\omega t - kz - \phi(z,t)]} + \text{c.c.}]$ on the right-hand side, Eq. (3) becomes

$$-2k\left(\frac{\partial E_0(z,t)}{\partial z} + \frac{1}{c}\frac{\partial E_0(z,t)}{\partial t}\right) = \mu_0\omega^2\text{Im}[P_0(z,t)]. \tag{5}$$

In quantum theory, the macroscopic polarization $P$ is given by the expectation value of the electric dipole moment $\hat{\mu}$; $\langle P(z,t)\rangle = N_s\text{Tr}\{\langle\rho(z,t)\cdot\mu\rangle\}$, where $N_s$ is the atomic density of the target molecules. Applied to the four-level system of CARS, the four components of $P$ can be written as $P_{0p}(z,t) = N_s\mu_{13}\rho_{13}(z,t)$, $P_{0s}(z,t) = N_s\mu_{23}\rho_{23}(z,t)$, $P_{0pr}(z,t) = N_s\mu_{24}\rho_{24}(z,t)$, and $P_{0as}(z,t) = N_s\mu_{14}\rho_{14}(z,t)$. Eliminating the space component by substituting $\frac{\partial}{\partial z} = \frac{1}{c}\frac{\partial}{\partial t}$ and using these expressions of polarizations, Eq. (5) casts into

$$\frac{1}{c}\frac{\partial E_q}{\partial t} = -N_s\mu_0\mu_{ij}\frac{E_q(t)}{\hbar}\text{Im}\rho_{ij}, \tag{6}$$

where $q = p, s, pr, as$ and $i, j$ are the indices of the states involved in the respective transitions.

The density matrix elements $\rho_{ij}$ are found from the Liouville–von Neumann equation $i\hbar\dot{\rho} = [H, \rho]$ with the Hamiltonian from Eq. (2). After applying the rotating-wave approximation and the adiabatic elimination of the excited states assuming that $\dot{\rho}_{13}, \dot{\rho}_{14}, \dot{\rho}_{23}, \dot{\rho}_{24}, \dot{\rho}_{34} \approx 0$, $\rho_{34} \approx 0$, $\rho_{33}, \rho_{44} \ll \rho_{11}, \rho_{22}$, and $\dot{\rho}_{33}, \dot{\rho}_{44} \approx 0$, and using the control condition on the chirp parameters $\alpha_s - \alpha_p = \alpha_{pr}$, the density matrix elements $\rho_{13}, \rho_{23}, \rho_{14}, \rho_{24}$ read in terms of $\rho_{11}$, $\rho_{22}$, and $\rho_{12}$ in the field interaction representation as follows:

$$\rho_{13} = \frac{1}{2(\Delta_s + \alpha_p t)}\Omega_{p0}(t)\rho_{11} + \frac{1}{2(\Delta_s + \alpha_p t)}\Omega_{s0}(t)\rho_{12},$$

$$\rho_{23} = \frac{1}{2(\Delta_s + \alpha_s t)}\Omega_{s0}(t)\rho_{22} + \frac{1}{2(\Delta_s + \alpha_s t)}\Omega_{p0}(t)\rho_{21},$$

$$\rho_{14} = \frac{1}{2\Delta_{as}}\Omega_{as0}(t)\rho_{11} + \frac{1}{2\Delta_{as}}\Omega_{pr0}(t)\rho_{12},$$

$$\rho_{24} = \frac{1}{2(\Delta_{as} + \alpha_{pr}t)}\Omega_{pr0}(t)\rho_{22} + \frac{1}{2(\Delta_{as} + \alpha_{pr}t)}\Omega_{as0}(t)\rho_{21}. \tag{7}$$

The details of the derivation of Eqs. (7) are presented in Appendix A. Furthermore, substituting Eq. (7) into Eq. (6) and rewriting the equations in terms of Rabi frequencies lead

to the following Maxwell's equations:

$$\frac{\partial\Omega_{p0}}{\partial t} = c\frac{\partial\Omega_{p0}}{\partial z} = -\frac{\eta}{2(\Delta_s + \alpha_p t)}\kappa_{13}\omega_p\Omega_{s0}(t)\text{Im}[\rho_{12}],$$

$$\frac{\partial\Omega_{s0}}{\partial t} = c\frac{\partial\Omega_{s0}}{\partial z} = \frac{\eta}{2(\Delta_s + \alpha_s t)}\kappa_{23}\omega_s\Omega_{p0}(t)\text{Im}[\rho_{12}],$$

$$\frac{\partial\Omega_{pr0}}{\partial t} = c\frac{\partial\Omega_{pr0}}{\partial z} = \frac{\eta}{2(\Delta_{as} + \alpha_{pr}t)}\kappa_{24}\omega_{pr}\Omega_{as0}(t)\text{Im}[\rho_{12}],$$

$$\frac{\partial\Omega_{as0}}{\partial t} = c\frac{\partial\Omega_{as0}}{\partial z} = -\frac{\eta}{2(\Delta_{as})}\kappa_{14}\omega_{as}\Omega_{pr0}(t)\text{Im}[\rho_{12}]. \tag{8}$$

Here, $\kappa_{ij} = N\mu_0\mu_{ij}^2c^2/(3\hbar)$, $N$ is the number density of molecules given by $N_A/V_0$ under the ideal gas conditions (where $N_A$ is Avogadro's number), $V_0$ is the molar volume, and $\eta$ is the fractional number density, which will be described in detail in the next section. The factor $1/3$ comes from the averaging over all orientations of the molecular dipole $\langle\mu_x\mu_y\rangle = \langle\mu_x\mu_z\rangle = \langle\mu_y\mu_z\rangle = 0$ and $\langle\mu_j\rangle = (1/3)\mu^2$, $j = x, y, z$ [37]. Considering the dipole moment of methanol $\mu_{ij} = 1.70D$, the constant $\kappa_{ij}$ is found to be $3.636 \times 10^{-3}[\omega_{21}]$.

Equations (8) coupled with the multilayer model described below are numerically solved using the transform-limited and the control pulse trains to find the scattered anti-Stokes signal. Note that the right-hand side of Eqs. (8), which describes the induced polarization in the target molecules, depends only on the imaginary part of coherence $\rho_{21}$ out of all density matrix elements. Thus the maximum value of this coherence provides the optimal amplitude of the scattered signal.

To analyze the impact of decoherence due to spontaneous decay and collisional dephasing of molecules, the Liouville–von Neumann equations are augmented by the relaxation terms. Spontaneous decay from state $|i\rangle$ to state $|j\rangle$ is denoted by $\gamma_{ij}$, while collisional dephasing between states $|i\rangle$ and $|j\rangle$ is denoted by $\Gamma_{ij}$. Spontaneous decay impacts state populations and coherence via the diagonal and off-diagonal reduced density matrix elements, respectively, while collisional dephasing is assumed to be weak enough not to change state populations but strong enough to cause dipole phase interruption via off-diagonal reduced density matrix elements. Vibrational energy relaxation [38,39] within the ground electronic state is accounted for through parameter $\gamma_{21}$. We neglect vibrational energy relaxation within the excited electronic state since the respective vibrational states $|3\rangle$ and $|4\rangle$ are negligibly populated during dynamics. Vibrational energy relaxation is an important topic in chemical physics, since it relates to fundamental reaction processes [40,41], conformational changes [42], or spectroscopic measurements [43,44], and its understanding is the first step toward controlling these phenomena.

$$\dot{\rho}_{11} = -i/\hbar[H,\rho]_{11} + \gamma_{21}\rho_{22} + \gamma_{31}\rho_{33} + \gamma_{41}\rho_{44}, \quad \dot{\rho}_{12} = -i/\hbar[H,\rho]_{12} - (\gamma_{21}/2 + \Gamma_{21})\rho_{12},$$

$$\dot{\rho}_{13} = -i/\hbar[H,\rho]_{13} - (\gamma_{31}/2 + \gamma_{32}/2 + \gamma_{21}/2 + \gamma_{41}/2 + \Gamma_{31})\rho_{13},$$

$$\dot{\rho}_{14} = -i/\hbar[H,\rho]_{14} - (\gamma_{41}/2 + \gamma_{42}/2 + \gamma_{21}/2 + \gamma_{31}/2 + \Gamma_{41})\rho_{14},$$

$$\dot{\rho}_{22} = -i/\hbar[H,\rho]_{22} - \gamma_{21}\rho_{22} + \gamma_{32}\rho_{33} + \gamma_{42}\rho_{44}, \quad \dot{\rho}_{23} = -i/\hbar[H,\rho]_{23} - (\gamma_{31}/2 + \gamma_{32}/2 + \gamma_{21}/2 + \gamma_{42}/2 + \Gamma_{32})\rho_{23},$$

$$\dot{\rho}_{24} = -i/\hbar[H,\rho]_{24} - (\gamma_{41}/2 + \gamma_{42}/2 + \gamma_{21}/2 + \gamma_{23}/2 + \Gamma_{42})\rho_{24}, \quad \dot{\rho}_{33} = -i/\hbar[H,\rho]_{33} - (\gamma_{31} + \gamma_{32})\rho_{33},$$

$$\dot{\rho}_{34} = -i/\hbar[H,\rho]_{34} - \Gamma_{43}\rho_{34}, \quad \dot{\rho}_{44} = -i/\hbar[H,\rho]_{44} - (\gamma_{41} + \gamma_{42})\rho_{44}. \tag{9}$$
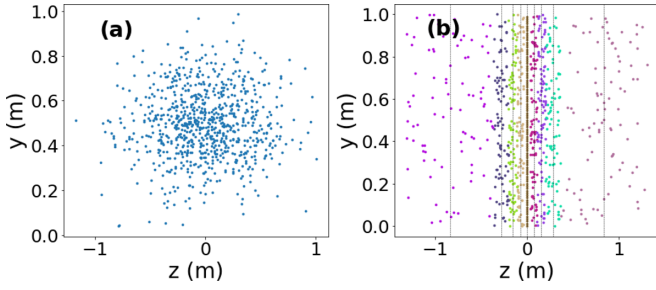
FIG. 2. The Gaussian distribution of the target molecules in (a) is based on the density of molecules and in (b) is converted into the multilayer model; molecules are given different colors to distinguish the layers. Each layer in the multilayer model is characterized by the fractional number density $\eta$ and the distance to its adjacent layer $(\Delta z)_\eta$. If $N_s$ is the number of the target molecules and $N$ is the number of total molecules associated with the layer, the fractional number density of that layer is defined as $\eta = N_s/N$. The distance between the adjacent layers $(\Delta z)_\eta$ changes according to the Gaussian distribution of molecules. The incoming pulses pass through a series of scattering events with the target molecules within each layer to produce a detectable backscattered CARS signal.

### B. The target molecules' distribution

We consider the target molecules as a cluster of molecules with its center located a large distance away from the source and its density following a Gaussian distribution. We introduce a multilayer model to analyze the propagation and scattering of the pump, Stokes, probe, and anti-Stokes pulses through this spatial distribution of molecules (Fig. 2). The model mimics the distribution of molecules in the air and allows us to solve the propagation and scattering tasks in an elegant and simple way. In this model, each layer is characterized by the fractional number density $\eta$ and the distance to its adjacent layer $(\Delta z)_\eta$. The distance between the layers changes according to the Gaussian distribution of molecules. If $N_s$ is the number of target molecules and $N$ is the number of total molecules associated with the layer, the fractional number density of that layer is defined as $\eta = N_s/N$. Suppose all target molecules in the central layer are arranged vertically next to each other with no background molecules between them; then the area occupied by these molecules is $S = \pi(d/2)^2 N_s$ giving $N_s = 4S/\pi d^2$, where $d$ is an approximate diameter of the target molecule. If $(\Delta z)_\eta$ is the width of this layer, the total number of molecules $N$ is $[S(\Delta z)_\eta/V_0]N_A$, where $V_0$ is the molar volume and $N_A$ is Avogadro's number. This gives

$$\eta = \frac{N_s}{N} = \frac{\frac{4S}{\pi d^2}}{\left(\frac{S(\Delta z)_\eta}{V_0}\right)N_A} = \frac{4V_0}{\pi d^2 (\Delta z)_\eta N_A}. \tag{10}$$

We consider $N_s$ to be constant within each layer. Now, we take $N = N_s$ for the central layer and calculate its width. For any subsequent layer the total number of molecules is different. Given $N_s$, the increase in the layer width by $\Delta z_\eta$ increases the layer's volume and thus decreases the target's density by the factor $(1 + \Delta z_\eta/\Delta z_0)$. The width of each sequential layer is calculated using Eq. (10). Consider that the density changes as per the Gaussian distribution function having the full width at half maximum (FWHM) $\sigma$ and its maximum value at the
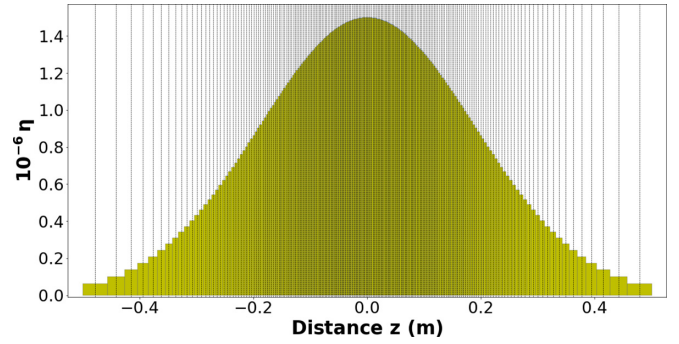


FIG. 3. An example of the multilayer model of a molecular distribution for the width of the Gaussian distribution in Eq. (11) of the target molecules $\sigma = 0.19$ m. Here, each of the 200 vertical lines represents the location of the scattering event, and the scattering layers become more dense as the density peaks at the center.

center $z_0$ of the cluster of molecules as

$$\eta = \frac{N_s V_0}{S N_A \sqrt{2\pi}\sigma} e^{-(z-z_0)^2/(2\sigma^2)}. \tag{11}$$

The maximum density $\eta_0$ of the central layer is found by substituting $z = z_0$ in Eq. (11). This value of $\eta$ is then substituted in Eq. (10) to find the width of the central layer $(\Delta z)_\eta = (\Delta z)_0$. Once we find the width of the central layer, the $\eta$ of the adjacent layer is found by substituting the new value of $z$, $z_0 + (\Delta z)_\eta$, in Eq. (11). This process is repeated to find the entire density distribution of the cluster of molecules. The distance between scattering layers $(\Delta z)_\eta$ increases towards both ends of the distribution. So we converted the three-dimensional cluster of molecules into a set of two-dimensional layers of molecules. Figure 3 shows a set of layers, the distance between them, and the density associated with each layer. In numerical calculations, we consider $\sigma = 0.2$ m with its center 1 km away from the source, which together with $\eta_0$ determines the total number of layers to be equal to 199.

### C. Propagation through the atmosphere

For completeness of the picture, it is necessary to take into account the effects of the atmosphere as pulses propagate through the molecular distribution. The propagation of femtosecond pulses through the atmosphere under various air conditions has been broadly investigated, e.g., Refs. [45,46]. Various effects during the propagation including the dispersion and the nonlinear self-focusing are not within the scope of this paper. We use Beer's law under the ideal conditions to account for the change in the amplitude of the pulses as they propagate through the atmosphere [47]. Assuming there is no turbulence and the air is homogeneous, the intensity of the pulse trains attenuates exponentially due to scattering and absorption as they propagate. The intensity $I$ as a function of the distance $z$ can be written as $I(z) = I_0 e^{-\beta_e z}$, where $\beta_e$ is the extinction coefficient that contains factors of both scattering and absorption. We use the clear air atmospheric coefficient of $0.55$ km$^{-1}$ in numerical calculations [48] shown in Sec. IV.

## III. A DEEP NEURAL NETWORK FOR EVALUATION OF THE PHASE OF THE FIELDS SCATTERED FROM THE TARGET MOLECULES

To investigate the controllability of population dynamics and vibrational coherence in the target molecules by propagating electromagnetic fields, we need to know the evolution of the key fields' parameters after each scattering event. This allows us to accurately calculate the quantum coherence and the induced polarization at the sequential steps of the numerical calculation. In the case of using the chirped pulse control scheme within the multilayer model of molecule distribution, the coupled Maxwell's and Liouville–von Neumann equations alter the initial, predetermined phase of the incident pulses impacting the response of the target molecules. Thus extracting the analytical phase from the numerical solutions of Eqs. (8) and verifying that the chirping scheme is applied to each scattering event become extremely important tasks for evaluating the response from the quantum system. To accomplish this goal, we developed a mechanism for classifying different kinds of pulses from the numerical data, based on their chirping, and extracting the chirp parameters from these classified pulses using a machine learning technique [49,50]. This approach of extracting the information about the phase of the pulses from the numerical grid and obtaining an accurate value of the chirp parameters may have a wide range of applications in quantum control and spectroscopy.

The machine learning model we created is the deep convolutional neural network (CNN). A CNN is built to classify a given pulse into one of three kinds: linear, quadratic, and the chirp shape according to our control scheme, namely, $\alpha_s = -\alpha_p$ and $\alpha_{pr} = \alpha_s - \alpha_p$ for $t \leqslant t_c$, and $\alpha_s = \alpha_p$ and $\alpha_{pr} = 0$ for $t > t_c$. Another CNN is built to do the regression work; it calculates the parameters of the fields and has a structure similar to that of the classification neural network. The structure will be discussed later in Appendix B.

Of principal importance for studying the phase of the numerical pulses is the availability of training data. A massive quantity of training data is a necessary requirement for deep learning training to concur a problem [51]. Since it is difficult to collect thousands of pieces of actual data from the experiments, we created a program that generated the scattered laser pulses randomly based on an arbitrary laser pulse model

$$E(t) = E_0 e^{-\frac{t^2}{2\tau^2}} \cos[\omega_L t + M(t)]. \tag{12}$$

Here, $\tau$ is the single-pulse duration, $E_0$ is the peak value of the field having the Gaussian envelope, and $\omega_L t + M(t)$ is the phase of the field having the modulation $M(t)$, which is the key to quantum control. A different parity of the phase modulation leads to different control scenarios [52,53]. Here, we present $M(t)$ as an expansion in the Taylor series

$$M(t) = a_0 + a_1 t^1 + a_2 t^2 + a_3 t^3 + \cdots. \tag{13}$$

Since in most cases the higher orders have a very limited contribution, we created data for three kinds of phase using terms up to the third power in time: The "linear" phase is determined by two parameters, the carrier frequency $a_1$ and the linear chirp $a_2$; then the field phase reads $\phi(t) = a_1 t + a_2 t^2$. The "second" phase is determined by three parameters, the carrier frequency $a_1$, the linear chirp $a_2$, and the second-order

chirp $a_3$; then the phase reads $\phi(t) = a_1 t + a_2 t^2 + a_3 t^3$. The "roof" phase comprises two parts, before central time and after, and is determined by three parameters, the carrier frequency $a_1$, the linear chirp $\tilde{a}_2$ for the first half of the pulse, and the linear chirp $\tilde{\tilde{a}}_2$ for the second half of the pulse; then the constructed phase of the field reads $\phi(t) = a_1 t + \tilde{a}_2 t^2$ for $t \leqslant 0$ and $\phi(t) = a_1 t + \tilde{\tilde{a}}_2 t^2$ for $t > 0$.

We simulated the pulses with these three kinds of phase using characteristic values of the field parameters and generated training data in the quantity of $5 \times 10^4$ for each kind by varying the carrier frequency and the chirp rate. During the training process, we applied the ADAM optimizer algorithm with a learning rate of 0.1 and regularization of 0.02 [54]. The loss function of the classification model is the cross entropy, but the mean-square error is the loss function for the regression model. The early stop technique was also used to control the overfitting [55]. The details of the construction of the neural networks for both the classification and the regression models are presented in Appendix B.

After training the classification and regression models, they are combined to be used as directed. The classification block classifies the random pulse and sends it to the corresponding regression block to solve for the analytical parameters of one of the three kinds of phase. The classification reaches an accuracy of 97.93%, and the overall root-mean-square error of the regression is smaller than 0.1, yielding to accurate enough results of the deep learning model. Both the classification and regression models are evaluated via a separate test data set, which contains $3 \times 10^3$ samples. To demonstrate the high accuracy of the analytical fit to the numerical data of the phase of the field, we show several prototypical phases in Fig. 4.

## IV. NUMERICAL RESULTS

Numerical analyses of the effects of the pulse shaping on the optimization of quantum coherence and mitigation of decoherence in the target molecules as well as the impact of multiple scattering from the target molecules are performed using the methanol molecule and addressing the Raman active symmetric mode having frequency 2837 cm$^{-1}$ (85.05 THz) [5]. This mode is chosen as a frequency unit ($\omega_{21}$). The control scheme provides the selectivity of excitation of Raman active modes with a resolution up to $1/\tau$, where $\tau$ is a chirped pulse duration, which is about 2–3 cm$^{-1}$. Thus the asymmetric stretch mode having frequency 2942 cm$^{-1}$ (88.20 THz) is not excited by the control scheme. The selectivity of excitation is not preserved when broadband but transform-limited pulse trains are applied.

First we present the results of the investigation of the dependence of the population and coherence on the peak Rabi frequency of the control pulses and reveal an adiabatic type of solution leading to the maximum vibrational coherence. Then we analyze the four-level system dynamics subject to the interaction with the control pulse trains in the presence of decoherence and demonstrate a sustainable value of vibrational coherence. Finally, we show the solution of the coupled Maxwell's and Liouville–von Neumann equations for the control pulse trains interacting with an ensemble of methanol molecules illustrating growth of
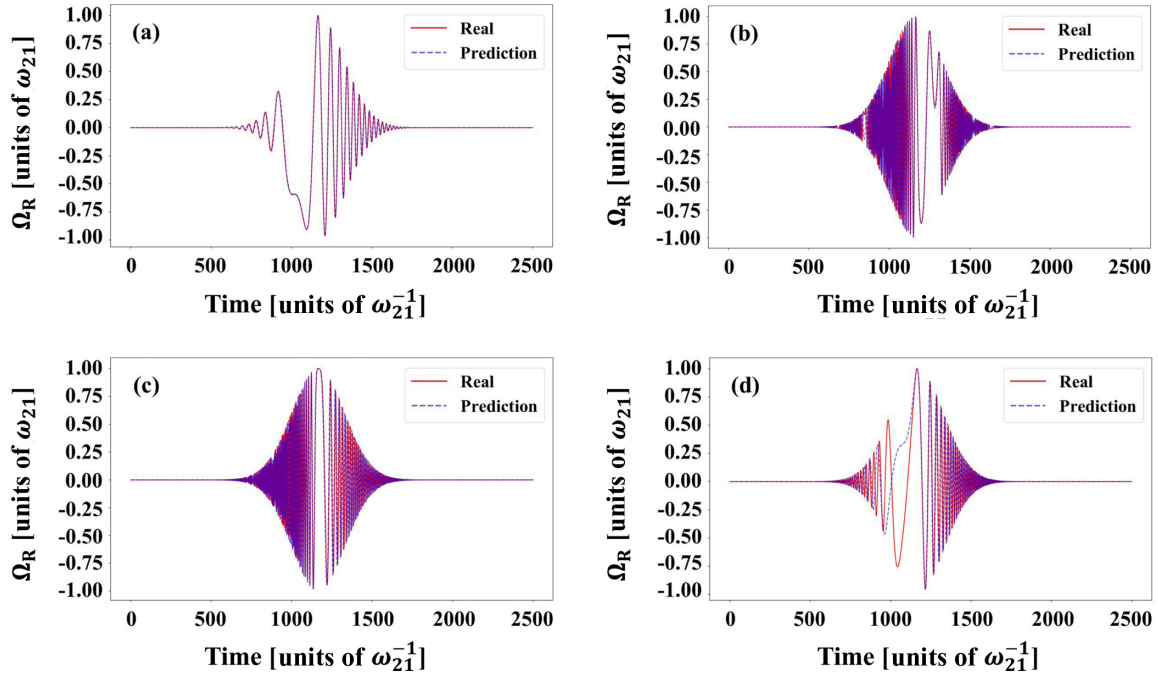
FIG. 4. Different shapes of the phase of the field obtained numerically (solid curve) and using the deep convolution neural network model (dashed curve) with different types of phase of the input pulse: (a) linear chirp, $\phi(t) = a_1 t + a_2 t^2$, both the real and predicted kinds are "linear", the real parameters are 3.00 and 0.60 and the predicted parameters are 3.02 and 0.61; (b) quadratic dependence of the phase on time having $a_2 < 0$ in $\phi(t) = a_1 t + a_2 t^2 + a_3 t^3$, both the real and predicted kinds are "second", the real parameters are 8.45, $-7.81$ and 1.69 and the predicted parameters are 8.43, $-7.76$ and 1.67; (c) "roof" chirp having positive chirp rate for the first part of the pulse and negative chirp rate for the second part of the pulse [36], $\phi(t) = a_1 t + \tilde{a}_2 t^2$ for $t \leqslant 0$, and $\phi(t) = a_1 t + \tilde{\tilde{a}}_2 t^2$ for $t > 0$, both the real and predicted kinds are "roof", the real parameters are 0.40, 9.28 and $-2.83$ and the predicted parameters are 0.29, 9.40 and $-2.96$; (d) quadratic dependence of the phase on time having $a_2 > 0$ in $\phi(t) = a_1 t + a_2 t^2 + a_3 t^3$, both the real and predicted kinds are "second", the real parameters are 2.00, 0.80 and 0.20 and the predicted parameters are 1.88, 1.01 and 0.18. Note that there is no discrepancy in the determination of the kind of phase; only the parameters have rare errors.

the vibrational coherence and the anti-Stokes component of the propagating fields. Where appropriate, we compare the results with those for the transform-limited pulse trains' interaction with the symmetric stretch mode in the CARS configuration.

## A. Analysis of the state population and coherence induced by the control pulses

Figures 5(a)–5(d) show the dependence of the populations and coherence as a function of the peak Rabi frequency for the case of the transform-limited pump, Stokes, and probe pulses with zero and nonzero one-photon detuning [Figs. 5(a) and 5(c)] and control pulses with zero and nonzero one-photon detuning [Figs. 5(b) and 5(d)], respectively. The envelope of the Rabi frequency is the same for all three transform-limited pulses, which are also used as an initial condition for chirping in the control scheme. The values of the Rabi frequency on the abscissa are presented for the transform-limited pulse. Decoherence is not taken into account to get a clear picture of the dependence of the state population and coherence on the Rabi frequencies. Under the one-photon resonance condition shown for the transform-limited pulses in Fig. 5(a) and for the chirped pulses in Fig. 5(b), the population of the excited

states is significant, which prevents us from achieving an equal population between the ground state $|1\rangle$ and the excited state $|2\rangle$. In the transform-limited pulse scenario in Fig. 5(a), coherence periodically becomes zero, which is not the case for the control pulse solution shown in Fig. 5(b). Such a behavior in Fig. 5(a) is due to the pulse area type of solution, when the probability amplitude of the states depends on the pulse area, with $\pi$ value leading to the population inversion and $2\pi$ value leading to the population return. In contrast, the control pulse scheme provides an adiabatic type of response in the four-level system with nonzero value of coherence, which depends on the strength of the fields as shown in Fig. 5(b). The one-photon detuning $\Delta_s = \Delta_{as} = \Delta = 1.0 \, \omega_{21}$ minimizes the transitional population of the excited states $|3\rangle$ and $|4\rangle$ for both the transform-limited pulse and the control pulse scenarios shown in Figs. 5(c) and 5(d), respectively. The one-photon detuning shifts the point of first zero coherence toward higher values of the Rabi frequencies in the transform-limited case in Fig. 5(c). In the control case in Fig. 5(d), the first point of equal population giving the maximum vibrational coherence occurs at the peak Rabi frequency $\Omega_{p0} = 0.75 \, \omega_{21}$ and is achieved due to two-photon adiabatic passage with a negligible involvement of the excited state manifold in the population dynamics. Beyond this point, the coherence value varies
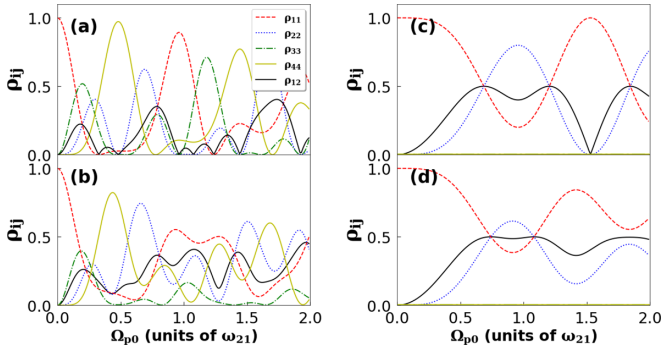
FIG. 5. The population and coherence in the four-level system as a function of the peak Rabi frequency $\Omega_p$ (units of $\omega_{21}$), which is the same for the pump, Stokes, and probe pulses, $\omega_{21} = 85$ THz. Parameters used in the calculations are $\tau_0 = 4.66\,\omega_{21}^{-1}$, $\Gamma = \gamma = 0$. In (a) the transform-limited pump, Stokes, and probe pulses with zero one-photon detuning are applied, $\Delta_s = \Delta_{as} = \Delta = 0$; in (b) the control pump, Stokes, and probe pulses with zero one-photon detuning are applied, $\alpha_s'/\tau_0^2 = -1.0$, $\Delta = 0$; in (c) the transform-limited pulses with nonzero one-photon detuning are applied, $\Delta = 1.0\,\omega_{21}$; and in (d), control pulses with nonzero one-photon detuning are applied, $\alpha_s'/\tau_0^2 = -1.0$, $\Delta = 1.0\,\omega_{21}$. Once coherence is built by the control pulses, it never drops to zero, in contrast to the transform-limited pulse solution. The detuned control scenario is robust for applications in CARS microscopy and spectroscopy because it provides a sustainable value of coherence resilient to fluctuations in the intensity of the Raman fields.

within the range from 0.5 to 0.35 for the peak Rabi frequency $\Omega_{p0} = 1\,\omega_{21}$ and higher. Once coherence is built, it never drops to zero, in contrast to the transform-limited pulse solution. Thus the detuned chirped pulse control scheme is more robust for applications in CARS microscopy and spectroscopy because it provides one with a sustainable value of coherence resilient to fluctuations in the intensity of the Raman fields. To demonstrate adiabatic passage generated under the condition of nonzero one-photon detuning, a time-dependent picture is presented in Figs. 6(a)–6(d). The time dependence of the population and coherence in the four-level system interacting with the transform-limited pump, Stokes, and probe pulses [Figs. 6(a) and 6(c)] and with the control pulses [Figs. 6(b) and 6(d)] shows the population dynamics and coherence for two values of the peak Rabi frequency $\Omega_p = 1.08$ and $1.5\,\omega_{21}$. The value of the Rabi frequency $\Omega_{p0} = 1.08\,\omega_{21}$ is chosen according to Fig. 5(d), which generates the second equal population between the ground state $|1\rangle$ and the excited state $|2\rangle$ and the maximum coherence $\rho_{21}$ in the control pulse scenario. This leads to adiabatic population transfer from the ground state $|1\rangle$ to the excited state $|2\rangle$. Meanwhile, the value of the peak Rabi frequency $\Omega_{p0} = 1.5\,\omega_{21}$ is chosen because it gives the first zero coherence for the transform-limited pulse scenario in Fig. 5(c), which is not the case for the control scheme in Fig. 5(d). Parameter $\gamma$ is nonzero in order to see how spontaneous decay impacts state dynamics for the chosen representative values of the Rabi frequency. The time dependence of the populations and a significant coherence are still observed in Fig. 6(d) demonstrating benefits of the control scheme.
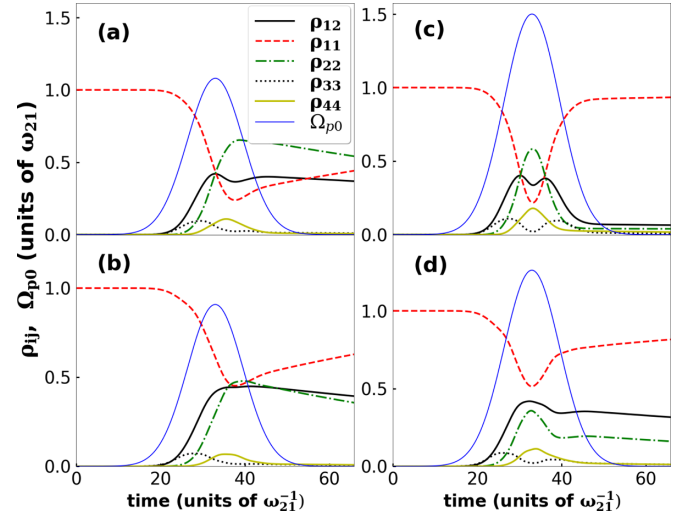


FIG. 6. Dynamics of the population of four states $\rho_{11}$ (dashed red curve), $\rho_{22}$ (dash-dotted green curve), $\rho_{33}$ (dotted black curve), and $\rho_{44}$ (solid yellow curve), and coherence $\rho_{21}$ (solid black curve), in the four-level system interacting with the transform-limited pump, Stokes, and probe pulses [(a) and (c)] and the control pulses [(b) and (d)]; $\alpha_s'/\tau_0^2 = -1.0$ for the peak Rabi frequency of the pump, the Stokes, and the probe pulses (before chirping for the control scheme); $\Omega_p = 1.08\,\omega_{21}$ in (a) and (b) and $1.5\,\omega_{21}$ in (c) and (d). Other parameters are $\tau_0 = 4.66\,\omega_{21}^{-1}$, all $\gamma_{ij} = \gamma = 1.176 \times 10^{-2}\,\omega_{21}$, $\Gamma = 0$, $\Delta = 1.0\,\omega_{21}$.

## B. Analysis of the four-level system dynamics subject to the interaction with the control pulse trains in the presence of decoherence

We analyze the impact of decoherence in the four-level system through its interaction with the control pump, Stokes, and probe pulse trains, each consisting of ten pulses, in Fig. 7. The results in Figs. 7(a)–7(d) are given for the peak Rabi frequency $\Omega_{p0} = 1.08\,\omega_{21}$, and the results in Figs. 7(e)–7(h) are given for $\Omega_{p0} = 1.5\,\omega_{21}$. The value $\Omega_{p0} = 1.08\,\omega_{21}$ provides the maximum coherence $(1/2)$ for the control pulse and a high value of coherence $(0.45)$ for the transform-limited pulse according to Figs. 5(c) and 5(d), and the value $\Omega_{p0} = 1.5\,\omega_{21}$ gives contrasting values of coherence for the control pulse and transform-limited pulse applications, 0.39 and 0.07, respectively. We analyze the controllability and sustenance of vibrational coherence in the four-level system subject to a fast spontaneous decay and collisions ($\sim 10$ fs); then we investigate the impact of vibrational relaxation considering the decay on the order of 1 ps and demonstrate how the loss of coherence due to this process may be mitigated by periodically restoring the population of the excited vibrational state $|2\rangle$ of the ground electronic state, and then we compare this result with the case when collisional dephasing is of the same order of magnitude ($\sim 1$ ps).

Fast spontaneous decay and collisional dephasing rates ($10^{14}$ Hz) of the transitional excited states $|3\rangle$ and $|4\rangle$ impact population dynamics and coherence even though these states are negligibly populated, as shown in Figs. 7(a) and 7(e). Here, populations and coherence $\rho_{21}$ are presented as a function of time for $\gamma_{4i} = \gamma_{3i} = \Gamma_{4i} = \Gamma_{3i} = 10^{14}$ Hz, $i = 1, 2$. The population of states $|1\rangle \approx 0.6$ and $|2\rangle \approx 0.4$ is stable
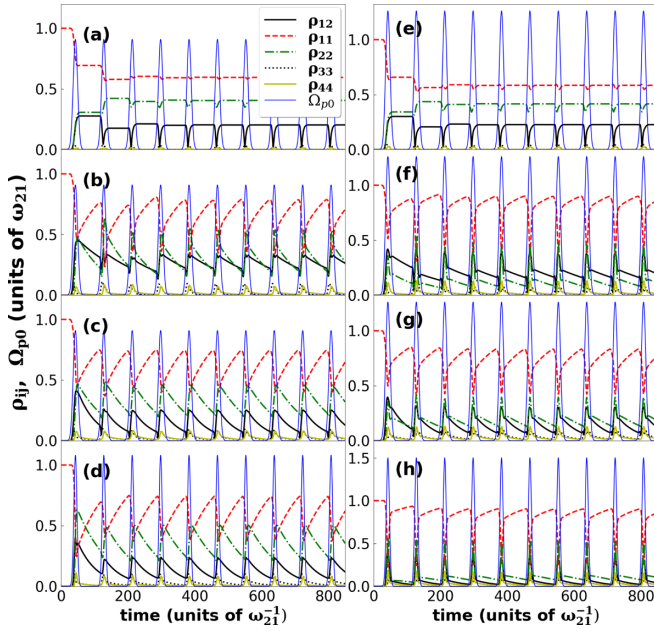
FIG. 7. Dynamics of the population of four states $\rho_{11}$ (dashed red curve), $\rho_{22}$ (dash-dotted green curve), $\rho_{33}$ (dotted black curve), and $\rho_{44}$ (solid yellow curve), and coherence $\rho_{21}$ (solid black curve), in the four-level system interacting with the control pulse trains having a repetition rate of 1 THz and value of the peak Rabi frequency in (a)–(d) equal to $\Omega_{p0} = 1.08\ \omega_{21}$ and in (e)–(h) equal to $\Omega_{p0} = 1.5\ \omega_{21}$. In (a) and (e), $\gamma_{4i} = \gamma_{3i} = \Gamma_{4i} = \Gamma_{3i} = 10^{14}$ Hz, $i = 1, 2$, but no vibrational relaxation, $\gamma_{21} = \Gamma_{21} = 0$; in (b) and (f), $\gamma_{4i} = \gamma_{3i} = \gamma_{21} = 10^{12}$ Hz and $\Gamma_{4i} = \Gamma_{3i} = \Gamma_{21} = 0$; in (c) and (g), $\gamma_{4i} = \gamma_{3i} = \Gamma_{4i} = \Gamma_{3i} = \gamma_{21} = \Gamma_{21} = 10^{12}$ Hz; and in (d) and (h) the four-level system interacting with the transform-limited pulse trains and $\gamma_{4i} = \gamma_{3i} = \Gamma_{4i} = \Gamma_{3i} = \gamma_{21} = \Gamma_{21} = 10^{12}$ Hz. The rest field parameters are $\tau_0 = 4.66\ \omega_{21}^{-1}$, $\Delta_s = \Delta_{as} = 1.0\ \omega_{21}$, and $\alpha'_s/\tau_0^2 = -1.0$ for the control pulse scenario.

between pulses; however, even though the $|3\rangle$ and $|4\rangle$ states are negligibly populated owing to the control scheme applied, their fast decoherence while the pulse is on (chirped pulse duration is 55 fs) impacts the populations of states $|2\rangle$ and $|1\rangle$, and the coherence $\rho_{21}$ periodically drops to $\sim 0.02$. Between pulses, such a fast relaxation from the excited states leads to a reduced but stable value of coherence $\rho_{21} \sim 0.2$.

Figures 7(b) and 7(f) show the system dynamics in the presence of the vibrational relaxation of state $|2\rangle$ described by $\gamma_{21} = 10^{12}$ Hz. Spontaneous decay from the excited states is also present: $\gamma_{4i} = \gamma_{3i} = \gamma_{21} = 10^{12}$ Hz; $\Gamma_{4i} = \Gamma_{3i} = \Gamma_{21} = 0$. Figures 7(b) and 7(f) demonstrate that coherence $\rho_{21}$ is periodically built up by the chirped pulses and then insignificantly reduces its value between the pulses in the trains. The spontaneous decay rate $\gamma = 1$ THz from the excited state $|4\rangle$ to $|3\rangle$ does not make any contribution to the population dynamics and was neglected. However, because the pulse train period is chosen to match the decay time $T = 1/\gamma_{21} = 1$ ps (and no collisional dephasing, $\Gamma_{ij} = 0$), the population of state $|2\rangle$ that decreased due to spontaneous decay is periodically restored by control fields providing a sustainable value of coherence. When vibrational relaxation is much faster (e.g., $10^{14}$ Hz) than the pulse repetition rate ($10^{12}$ Hz), coherence $\rho_{21}$ becomes

negligibly small between pulses (not shown here). Switching on collisional dephasing such that $\Gamma_{21} = \gamma_{21} = 1$ THz results in a more dramatic reduction of coherence $\rho_{21}$ as is shown in Figs. 7(c) and 7(g) because collisional dephasing cannot be mitigated by this mechanism being represented by off-diagonal density matrix elements. However, the resultant coherence $\rho_{21}$ does not drop to zero between pulses. This is due to the choice of the pulse repetition rate as well as the control scheme leading to a negligible population of the excited states $|3\rangle$ and $|4\rangle$ in the dynamics. In contrast, the simultaneous application of the transform-limited pump, Stokes, and probe pulse trains shown in Figs. 7(d) and 7(h) results in strong dependence of coherence on the peak Rabi frequency in accordance with the pulse area solution. The simultaneous application of the transform-limited pulses in this calculation aims to provide a comparison with the chirped pulse scenario. {Note that within a different control scheme, e.g., fractional stimulated Raman adiabatic passage (F-STIRAP) [56], which imposes a time delay between the Stokes and the pump pulses, the transform-limited pulses generate the maximum coherence.}The results of the calculations presented in Fig. 7 for various values of the Rabi frequency of the control pulses and the transform-limited pulses lead to the conclusion that for the control scheme there is vibrational coherence in the system for any value of the peak Rabi frequency within the adiabatic range, while for the related transform-limited pulse scenario this is not the case.

### C. The impact of Beer's law on the average intensity of the propagating anti-Stokes signal

We apply Beer's law under the ideal conditions to evaluate the change in the amplitude of the anti-Stokes signal as pulses propagate through the atmosphere. We apply ten transform-limited pulses in the pulse train. Numerical analysis shows that the amplitude of the pump, Stokes, and probe pulse trains is reduced upon propagation, while the average intensity of the anti-Stokes pulse trains is amplified as shown in Fig. 8 for propagation through 699 layers for both cases, with and without impact from the air. The intensity of the anti-Stokes pulse trains in the presence of the air is depreciated due to the scattering and absorption effects.

### D. Analysis of the coupled Maxwell's and Liouville–von Neumann equations and demonstration of the generation of an anti-Stokes signal

Using Maxwell's equations (8) coupled to the Liouville–von Neumann equations (9), we numerically analyzed the propagation effects of the control pump, Stokes, probe, and generated anti-Stokes fields scattered from the target molecules and observed the amplification of the anti-Stokes component. A machine learning approach was implemented to reveal the modulation of the phase of four field components after each scattering. Figure 9 shows the control pump, Stokes, probe, and built-up anti-Stokes pulses after each of five consecutive scattering events for the parameters of the fields $\Omega_{p(s,pr)} = 85$ THz ($E_{p(s,pr)_0} \sim 1.6 \times 10^9$ V/m), $\tau_0 = 54.8$ fs, $\alpha_s = -7$ THz/fs, and $\Delta_s = \Delta_{as} = \Delta = 850$ THz. The neural networks explained in the previous section were optimized
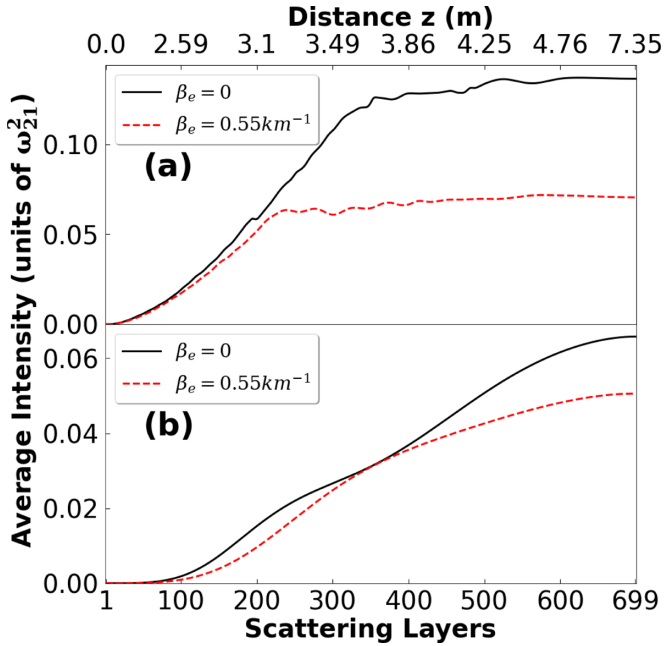
FIG. 8. Average intensity of the anti-Stokes pulses as a function of the number of scattering layers calculated applying Beer's law to the propagation of a transform-limited pulse train consisting of ten pulses. The black solid curve represents the change in the average intensity as pulses undergo scattering through layers for the case of $\beta_e = 0$ (without taking air into consideration), and the red dashed curve shows the case of $\beta_e = 0.55$ km$^{-1}$. The one-photon detuning is $\Delta = 1$ $\omega_{21}$ in (a) and $\Delta = 10$ $\omega_{21}$ in (b). The standard deviation of the target molecules' distribution is $\sigma = 1$ m. The depreciation of intensity is due to scattering and absorption in the air.

to work for these parameters. The classifier neural network predicted the pulses to be the third kind described above, and the regression neural network provided the chirping parameters. After five scattering events, the change in the initial chirp rate $\alpha_s$ is less than 0.001% indicating that the control scheme would work for a large number of layers. The anti-Stokes component is built up having the peak Rabi frequency about $10^{-6}\Omega_p$ after the fifth iteration.

We also analyzed propagation effects using the transform-limited pump, Stokes, and probe pulse trains having the peak Rabi frequency $\Omega_{p(s,pr)} = 85$ THz $= \omega_{21}$ and being largely detuned from the one-photon transitions; the detuning is $\Delta_s = \Delta_{as} = \Delta = 10$ $\omega_{21} = 850$ THz for the adiabatic regime (Fig. 10). We consider ten pulses in the pulse train having period $T = 1$ ps. The increase in the peak value of the anti-Stokes Rabi frequency $\Omega_{as}(t)$ by two orders of magnitude is observed 1 m (199 layers) away from the peak molecular density. The coherence is increasing from pulse to pulse, and the population is adiabatically transferred from the ground state $|1\rangle$ to the excited state $|2\rangle$ in the four-level system during the interaction with four fields in the CARS configuration. Here, an adiabatic regime is achieved due to a large one-photon detuning $\Delta = 10$ $\omega_{21}$ and the choice of the peak Rabi frequency $\Omega_{p(s,pr)} = \omega_{21}$, which result in a negligible population of the transitional states $|3\rangle$ and $|4\rangle$.

From the results above it follows that the implementation of the control pulse trains in the four-wave mixing in
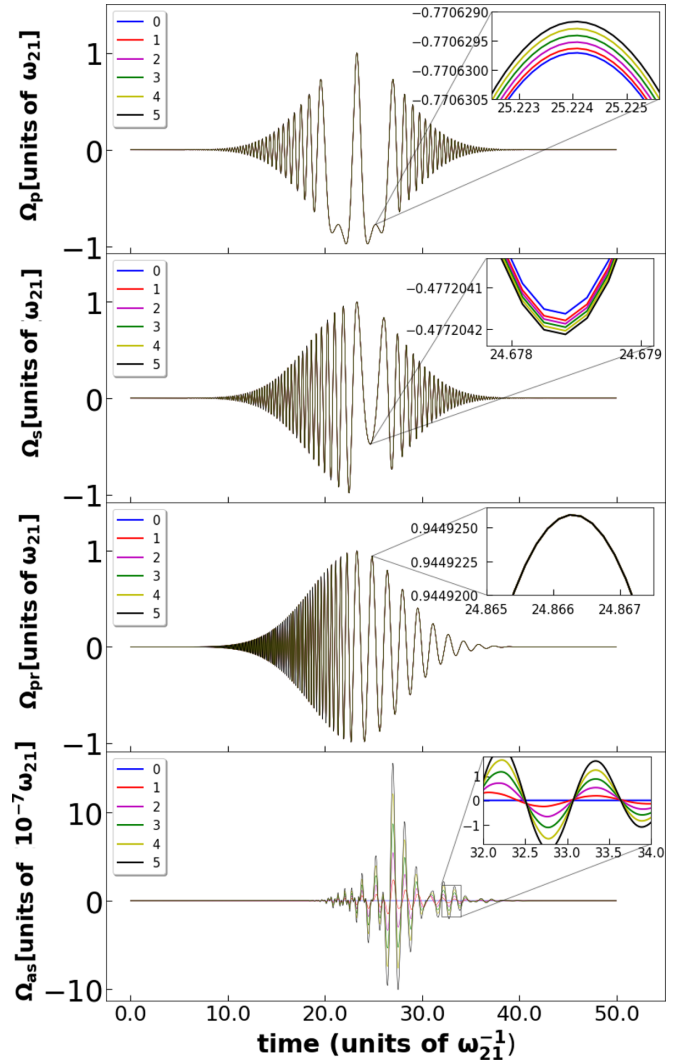


FIG. 9. The pump, the Stokes, the probe, and the built-up anti-Stokes chirped pulses after each of five consecutive scattering events. Here, 0, 1, 2, 3, 4, and 5 represent the incoming, first, second, third, fourth, and fifth scattering events, respectively. The incident pulses are chirped in accordance with the control scheme. The parameters of the fields are $\Omega_{p(s,pr)} = 85$ THz ($E_{p(s,pr)_0} \sim 1.6 \times 10^9$ V/m), $\tau_0 = 54.8$ fs, $\alpha_s = -7$ THz/fs, and $\Delta_s = \Delta_{as} = \Delta = 850$ THz. The anti-Stokes field is built up gradually and constitutes $\sim 10^{-6}$ of the amplitude of the incident field.

CARS is more robust for the generation of a sustainable anti-Stokes backscattered signal compared with the use of a set of transform-limited pulses. This is due to the adiabatic regime of light-matter interaction, which preserves vibrational coherence and facilitates a buildup of the anti-Stokes signal. For the case in which the phase-matching conditions are relaxed, given that the size of the molecules is less than the wavelength of the incident fields, a collinear copropagating configuration of CARS may be created using methanol as a surrogate target. Because the anti-Stokes radiation is generated as a result of the stimulated Raman scattering process, it is highly directional and is built up in the forward and the backward directions dominantly [22,57]. Therefore the backscattered anti-Stokes signal will reach a detector near the laser source.
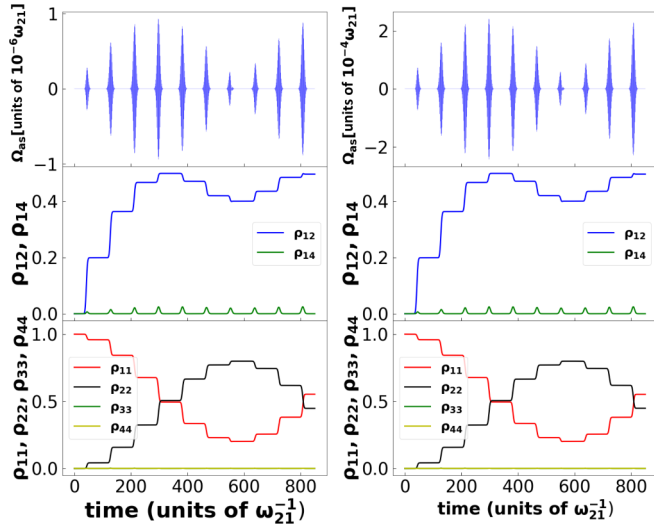
FIG. 10. Scattering dynamics using the transform-limited pump, Stokes, and probe pulse trains having the peak Rabi frequency equal to the frequency between states $|1\rangle$ and $|2\rangle$, $\Omega_{p(s,pr)_0} = \omega_{21}$, and being largely detuned from the one-photon transitions; the detuning is $\Delta_s = \Delta_{as} = \Delta = 10\,\omega_{21} = 850$ THz for the adiabatic regime. There are ten pulses in each pulse train. The first column shows ten anti-Stokes pulses (top), the state coherence (middle), and populations (bottom) after the first scattering event; the second column shows the same after the 199th scattering event. Parameters: $\sigma = 0.2$ m; 199 layers provide a distance of 1 m away from the peak molecular density; $\tau_0 = 54.8$ fs; $T = 1$ ps.

The following parameters of the fields may be used in an experiment: a pulse duration of the order of 100 fs, a peak field amplitude of $E_{0p(s,pr)} \sim 1.6 \times 10^9$ V/m; control pulse chirps obeying the relationship $\alpha_s = -\alpha_p$, $\alpha_{pr} = \alpha_s - \alpha_p$ for the first half of the pulse duration, $t \leqslant t_c$, and obeying $\alpha_s = \alpha_p$, $\alpha_{pr} = 0$ for $t > t_c$; a value of $\alpha_s = -7$ THz/fs, a pulse train period of the order of the spontaneous decay time, and a one-photon detuning of the order of $\Delta \sim 1$ fs$^{-1}$.

## V. SUMMARY

We present a semiclassical theory of the four-wave mixing process in coherent anti-Stokes Raman scattering implementing control pulse trains. The theory is based on a set of Maxwell's equations for propagation of the pump, the Stokes, the probe, and the anti-Stokes components of the fields coupled to the Liouville–von Neumann equations with relaxation for dynamics in the target molecules. It is intended for investigations of the remote detection of biochemical molecules. A multilayer model is developed to account for the spatial distribution of the target molecules in the air mimicking the environmental conditions. A machine learning approach is developed to analyze the evolving phase of the pulse trains as they undergo scattering within each layer. The approach makes use of the deep convolutional neural network. The quantum control method for the incident pulse shaping is implemented, which optimizes the macroscopic induced polarization in the target molecules by maximizing vibrational coherence. The method implies chirping of the incident pulse trains, which induce adiabatic population transfer within four
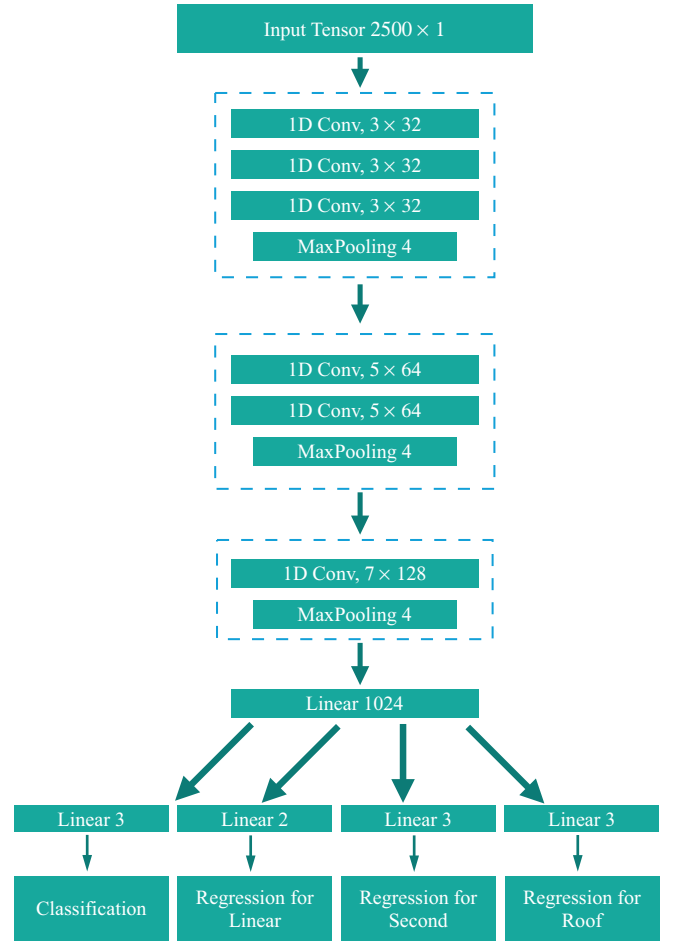


FIG. 11. The structure of the deep neural network. The same structure is shared by the phase type classifier and the three phase value regression models, except for the last output layer. Three convolutional blocks are used sequentially to extract the highly nonlinear information from the input time-dependent tensor. The linear layer is used after flattening the output from the last convolutional block. Conv, convolution; MaxPooling, maximum pooling.

states in the CARS scheme leading to a sustainable, high vibrational coherence. Importantly, the transitional excited states get negligibly populated, thus minimizing the impact of spontaneous decay and associated losses of coherence from these states. Moreover, the choice of the pulse train period to match the spontaneous decay time permits for mitigation of the vibrational decay. Enhancement of the anti-Stokes field is observed upon propagation through the ensemble of target molecules, achieved by the control pulse trains as well as by the transform-limited pulse trains with a large detuning and a carefully chosen Rabi frequency. The coherent enhancement of the anti-Stokes signal and mitigation of decoherence by chirped control fields form a foundation for the propagation of the anti-Stokes signal through distances on a kilometer scale.

## APPENDIX A: DERIVATION OF COUPLED MAXWELL'S AND LIOUVILLE–VON NEUMANN EQUATIONS

Maxwell's equations, with no free currents or charges, read

$$\nabla \cdot (\epsilon_0 E + P) = 0, \tag{A1}$$

$$\nabla \times E = -\partial B/\partial t, \tag{A2}$$

$$\nabla \times B = \mu_0 \partial (\epsilon_0 + P)/\partial t, \tag{A3}$$

$$\nabla \cdot B = 0. \tag{A4}$$

From Eqs. (A2) and (A3) we obtain the wave equation

$$\nabla^2 E - \epsilon_0 \mu_0 \frac{\partial^2 E}{\partial^2 t} = \nabla(\nabla \cdot E) + \mu_0 \frac{\partial^2 P}{\partial^2 t}. \tag{A5}$$

It follows from Eq. (A1) that $\nabla \cdot E = \nabla \cdot P/\epsilon_0$ in a space free from charges. In a plane-wave limit, when the wavelength is much less than the beam radius and neglecting any diffraction effects in the transverse direction, fields propagate in the $\hat{z}$ direction and have polarization in the $XY$ plane. Then $\nabla \cdot P$ may be set to zero, and the wave equation reads

$$\left(\frac{\partial}{\partial z} + \frac{1}{c}\frac{\partial}{\partial t}\right)\left(-\frac{\partial}{\partial z} + \frac{1}{c}\frac{\partial}{\partial t}\right)E = -\mu_0\frac{\partial^2 P}{\partial t^2}. \tag{A6}$$

Assuming the field is $E(z,t) = \frac{1}{2}[E_0(z,t)e^{-i[\omega t - kz - \phi(z,t)]} +$ c.c.] and polarization is $P(z,t) = \frac{1}{2}[P_0(z,t)e^{-i[\omega t - kz - \phi(z,t)]} +$ c.c.] and considering $E_0(z,t)$ and $\phi(z,t)$ as slowly varying functions of position and time, we write

$$-\frac{\partial E(z,t)}{\partial z} = -\frac{1}{2}[e^{-i\omega t}e^{ikz}e^{i\phi(z,t)}\frac{\partial E_0(z,t)}{\partial z} + ikE_0(z,t)e^{-i\omega t}e^{ikz}e^{i\phi(z,t)} + i\frac{\partial \phi(z,t)}{\partial z}E_0(z,t)e^{-i\omega t}e^{ikz}e^{i\phi(z,t)} + \text{c.c.}], \tag{A7}$$

$$\frac{1}{c}\frac{\partial E(z,t)}{\partial t} = \frac{1}{2c}[e^{-i\omega t}e^{ikz}e^{i\phi(z,t)}\frac{\partial E_0(z,t)}{\partial t} - i\omega E_0(z,t)e^{-i\omega t}e^{ikz}e^{i\phi(z,t)} + i\frac{\partial \phi(z,t)}{\partial t}E_0(z,t)e^{-i\omega t}e^{ikz}e^{i\phi(z,t)} + \text{c.c.}]. \tag{A8}$$

Then

$$\left(-\frac{\partial}{\partial z} + \frac{1}{c}\frac{\partial}{\partial t}\right)E = -\frac{ik}{2}[E_0(z,t)e^{-i\omega t}e^{ikz}e^{i\phi(z,t)} - \text{c.c.}] - \frac{i\omega}{2c}[E_0(z,t)e^{-i\omega t}e^{ikz}e^{i\phi(z,t)} - \text{c.c.}]$$

$$= -ik[E_0(z,t)e^{-i[\omega t - kz - \phi(z,t)]} - \text{c.c.}]$$

$$= -2ik\,\text{Im}E. \tag{A9}$$

By substituting Eq. (A9) into Eq. (A6), using $\omega/c = k$, and later assuming real fields we arrive at

$$-ik\left(\frac{\partial}{\partial z} + \frac{1}{c}\frac{\partial}{\partial t}\right)[E_0(z,t)e^{-i[\omega t - kz - \phi(z,t)]} + \text{c.c.}]$$

$$= -ik\frac{\partial E_0(z,t)}{\partial z}e^{-i[\omega t - kz - \phi(z,t)]} + ik\frac{\partial E_0^*(z,t)}{\partial z}e^{i[\omega t - kz - \phi(z,t)]} - \frac{ik}{c}\frac{\partial E_0(z,t)}{\partial t}e^{-i[\omega t - kz - \phi(z,t)]} + \frac{ik}{c}\frac{\partial E_0^*(z,t)}{\partial t}e^{i[\omega t - kz - \phi(z,t)]}$$

$$= -ik\left[\left(\frac{\partial E_0(z,t)}{\partial z} + \frac{1}{c}\frac{\partial E_0(z,t)}{\partial t}\right)e^{-i[\omega t - kz - \phi(z,t)]} - \left(\frac{\partial E_0^*(z,t)}{\partial z} + \frac{1}{c}\frac{\partial E_0^*(z,t)}{\partial t}\right)e^{i[\omega t - kz - \phi(z,t)]}\right]$$

$$= -2k\left(\frac{\partial E_0(z,t)}{\partial z} + \frac{1}{c}\frac{\partial E_0(z,t)}{\partial t}\right)\frac{1}{2i}\left(-e^{-i[\omega t - kz - \phi(z,t)]} + e^{i[\omega t - kz - \phi(z,t)]}\right)$$

$$= -2k\left(\frac{\partial E_0(z,t)}{\partial z} + \frac{1}{c}\frac{\partial E_0(z,t)}{\partial t}\right)\sin[\omega t - kz - \phi(z,t)]$$

$$= -\mu_0\frac{\partial^2}{\partial t^2}P(z,t). \tag{A10}$$

For $P(z,t) = \frac{1}{2}[P_0(z,t)e^{-i[\omega t - kz - \phi(z,t)]} + \text{c.c.}]$,

$$\frac{\partial^2}{\partial t^2}P(z,t) = -\omega^2\left(\frac{1}{2}[P_0(z,t)e^{-i[\omega t - kz - \phi(z,t)]} + \text{c.c.}]\right) = -\omega^2\text{Re}[P(z,t)]. \tag{A11}$$

Substituting these into Eq. (A10) gives

$$-2k\left(\frac{\partial E_0(z,t)}{\partial z} + \frac{1}{c}\frac{\partial E_0(z,t)}{\partial t}\right)\sin[\omega t - kz - \phi(z,t)]$$

$$= \mu_0\omega^2\{\text{Re}[P_0(z,t)]\cos(\omega t - kz) + \text{Im}[P_0(z,t)]\sin[\omega t - kz - \phi(z,t)]\}, \tag{A12}$$

leading to

$$-2k\left(\frac{\partial E_0(z,t)}{\partial z} + \frac{1}{c}\frac{\partial E_0(z,t)}{\partial t}\right) = \mu_0\omega^2\text{Im}[P_0(z,t)]. \tag{A13}$$

In quantum theory, a measurable quantity is the expectation value, which for macroscopic polarization is an expectation value of the electric dipole moment operator $\hat{\mu}$, $\langle P(z,t) \rangle = N_s \mathrm{Tr}\{\langle \rho(z,t) \cdot \mu \rangle\}$, where $N_s$ is the atomic density of the target molecules. Applied to the four-level system of CARS, it contains four components corresponding to each of the four transitions:

$$P_p(z,t) = 2N_s \mathrm{Re}[\mu_{13}\rho_{13}(z,t)e^{i[\omega_p t - k_p z - \phi(z,t)]}], \quad P_s(z,t) = 2N_s \mathrm{Re}[\mu_{23}\rho_{23}(z,t)e^{i[\omega_s t - k_s z - \phi(z,t)]}],$$

$$P_{pr}(z,t) = 2N_s \mathrm{Re}[\mu_{24}\rho_{24}(z,t)e^{i[\omega_{pr} t - k_{pr} z - \phi(z,t)]}], \quad P_{as}(z,t) = 2N_s \mathrm{Re}[\mu_{14}\rho_{14}(z,t)e^{i[\omega_{as} t - k_{as} z - \phi(z,t)]}], \tag{A14}$$

giving $P_{0p}(z,t) = N_s\mu_{13}\rho_{13}(z,t)$, $P_{0s}(z,t) = N_s\mu_{23}\rho_{23}(z,t)$, $P_{0pr}(z,t) = N_s\mu_{24}\rho_{24}(z,t)$, and $P_{0as}(z,t) = N_s\mu_{14}\rho_{14}(z,t)$.

For the four components of propagating fields in CARS, Eq. (A13) reads as follows:

$$\frac{\partial E_p}{\partial z} + \frac{1}{c}\frac{\partial E_p}{\partial t} = -N_s \frac{\mu_0\mu_{13}\omega_p^2}{k_p}\mathrm{Im}\rho_{13}(z,t), \quad \frac{\partial E_s}{\partial z} + \frac{1}{c}\frac{\partial E_s}{\partial t} = -N_s \frac{\mu_0\mu_{23}\omega_s^2}{k_s}\mathrm{Im}\rho_{23}(z,t),$$

$$\frac{\partial E_{pr}}{\partial z} + \frac{1}{c}\frac{\partial E_{pr}}{\partial t} = -N_s \frac{\mu_0\mu_{24}\omega_{pr}^2}{k_{pr}}\mathrm{Im}\rho_{24}(z,t), \quad \frac{\partial E_{as}}{\partial z} + \frac{1}{c}\frac{\partial E_{as}}{\partial t} = -N_s \frac{\mu_0\mu_{14}\omega_{as}^2}{k_{as}}\mathrm{Im}\rho_{14}(z,t). \tag{A15}$$

If $\bar{t} = (t - \frac{z}{c})$, then $\frac{dt}{dz} = (\frac{d\bar{t}}{dz} + \frac{1}{c})$, which leads to $\frac{\partial}{\partial z} = \frac{\partial}{\partial t}\frac{\partial t}{\partial z} = \frac{1}{c}\frac{\partial}{\partial t}$. Taking into account that $k_q = \omega_q/c$ and $c\omega_q\hbar = E_q$, where $q = p, s, pr, as$, Eq. (A15) becomes

$$\frac{1}{c}\frac{\partial E_q}{\partial t} = -N_s\mu_0\mu_{ij}\frac{E_q(t)}{\hbar}\mathrm{Im}\rho_{ij}. \tag{A16}$$

We find the density matrix elements $\rho_{ij}$ from the Liouville–von Neumann equation $i\hbar\dot{\rho} = [H, \rho]$ and using the above Hamiltonian in Eq. (2). We start by opening the commutator and applying the substitutions

$$\rho_{12} = \tilde{\rho}_{12}e^{i(\alpha_p - \alpha_s)t^2/2}, \quad \rho_{13} = \tilde{\rho}_{13}e^{i(\Delta_s t + \alpha_p t^2/2)}, \quad \rho_{14} = \tilde{\rho}_{14}e^{i\Delta_{as}t}, \quad \rho_{23} = \tilde{\rho}_{23}e^{i(\Delta_s t + \alpha_s t^2/2)},$$

$$\rho_{24} = \tilde{\rho}_{24}e^{i(\Delta_{as}t + \alpha_{pr}t^2/2)}, \quad \rho_{34} = \tilde{\rho}_{34}e^{i(\Delta_{as} - \Delta_s)t - i\alpha_p t^2/2}. \tag{A17}$$

Next, we apply the rotating-wave approximation and use the control condition on the chirp parameters $\alpha_s - \alpha_p = \alpha_{pr}$, and we arrive at

$$\dot{\rho}_{11} = -i\Omega_{p0}(t)/2\tilde{\rho}_{31} + i\Omega_{p0}^*(t)/2\tilde{\rho}_{13} - i\Omega_{as0}(t)/2\tilde{\rho}_{41} + i\Omega_{as0}^*(t)/2\tilde{\rho}_{14},$$

$$\dot{\rho}_{22} = -i\Omega_{s0}(t)/2\tilde{\rho}_{32} + i\Omega_{s0}^*(t)/2\tilde{\rho}_{23} - i\Omega_{pr0}(t)/2\tilde{\rho}_{42} + i\Omega_{pr0}^*(t)/2\tilde{\rho}_{24},$$

$$\dot{\rho}_{33} = i\Omega_{p0}(t)/2\tilde{\rho}_{31} - i\Omega_{p0}^*(t)/2\tilde{\rho}_{13} + i\Omega_{s0}(t)/2\tilde{\rho}_{32} - i\Omega_{s0}^*(t)/2\tilde{\rho}_{23},$$

$$\dot{\rho}_{44} = i\Omega_{as0}(t)/2\tilde{\rho}_{41} - i\Omega_{as0}^*(t)/2\tilde{\rho}_{14} + i\Omega_{pr0}(t)/2\tilde{\rho}_{42} - i\Omega_{pr0}^*(t)/2\tilde{\rho}_{24},$$

$$\dot{\tilde{\rho}}_{12} = i\alpha_{pr}t\tilde{\rho}_{12} - i\Omega_{p0}(t)/2\tilde{\rho}_{32} - i\Omega_{as0}(t)/2\tilde{\rho}_{42} + i\Omega_{s0}^*(t)/2\tilde{\rho}_{13} + i\Omega_{pr0}^*(t)/2\tilde{\rho}_{14},$$

$$\dot{\tilde{\rho}}_{13} = -i(\Delta_s + \alpha_p t)\tilde{\rho}_{13} - i\Omega_{p0}(t)/2(\rho_{33} - \rho_{11}) - i\Omega_{as0}(t)/2\tilde{\rho}_{43} + i\Omega_{s0}(t)/2\tilde{\rho}_{12},$$

$$\dot{\tilde{\rho}}_{14} = -i\Delta_{as}\tilde{\rho}_{14} - i\Omega_{p0}(t)/2\tilde{\rho}_{34} - i\Omega_{as0}(t)/2(\rho_{44} - \rho_{11}) + i\Omega_{pr0}(t)/2\tilde{\rho}_{12},$$

$$\dot{\tilde{\rho}}_{23} = -i(\Delta_s + \alpha_s t)\tilde{\rho}_{23} - i\Omega_{s0}(t)/2(\rho_{33} - \rho_{22}) - i\Omega_{pr0}(t)/2\tilde{\rho}_{43} + i\Omega_{p0}(t)/2\tilde{\rho}_{21},$$

$$\dot{\tilde{\rho}}_{24} = -i(\Delta_{as} + \alpha_{pr}t)\tilde{\rho}_{24} - i\Omega_{pr0}(t)/2(\rho_{44} - \rho_{22}) - i\Omega_{s0}(t)/2\tilde{\rho}_{34} + i\Omega_{as0}(t)/2\tilde{\rho}_{21},$$

$$\dot{\tilde{\rho}}_{34} = i(\Delta_s - \Delta_{as} + \alpha_p t)\tilde{\rho}_{34} - i\Omega_{p0}^*(t)/2\tilde{\rho}_{14} - i\Omega_{s0}^*(t)/2\tilde{\rho}_{24} + i\Omega_{as0}(t)/2\tilde{\rho}_{31} + i\Omega_{pr0}(t)/2\tilde{\rho}_{32}.$$

After performing adiabatic elimination of the excited states assuming that $\dot{\rho}_{13}, \dot{\rho}_{14}, \dot{\rho}_{23}, \dot{\rho}_{24}, \dot{\rho}_{34} \approx 0$, $\rho_{34} \approx 0$, $\rho_{33}, \rho_{44} \ll \rho_{11}, \rho_{22}$, and $\dot{\rho}_{33}, \dot{\rho}_{44} \approx 0$, the density matrix elements $\rho_{13}, \rho_{23}, \rho_{14}, \rho_{24}$ read in terms of $\rho_{11}, \rho_{22}$, and $\rho_{12}$ as follows:

$$\rho_{13} = \frac{1}{2(\Delta_s + \alpha_p t)}\Omega_{p0}(t)\rho_{11} + \frac{1}{2(\Delta_s + \alpha_p t)}\Omega_{s0}(t)\rho_{12},$$

$$\rho_{23} = \frac{1}{2(\Delta_s + \alpha_s t)}\Omega_{s0}(t)\rho_{22} + \frac{1}{2(\Delta_s + \alpha_s t)}\Omega_{p0}(t)\rho_{21},$$

$$\rho_{14} = \frac{1}{2\Delta_{as}}\Omega_{as0}(t)\rho_{11} + \frac{1}{2\Delta_{as}}\Omega_{pr0}(t)\rho_{12},$$

$$\rho_{24} = \frac{1}{2(\Delta_{as} + \alpha_{pr}t)}\Omega_{pr0}(t)\rho_{22} + \frac{1}{2(\Delta_{as} + \alpha_{pr}t)}\Omega_{as0}(t)\rho_{21}. \tag{A18}$$

Substituting Eq. (A18) into Eq. (A16) and rewriting the equations in terms of Rabi frequencies provide the following Maxwell's equations:

$$\frac{\partial \Omega_{p0}}{\partial t} = c\frac{\partial \Omega_{p0}}{\partial z} = -\frac{\eta}{2(\Delta_s + \alpha_p t)}\kappa_{13}\omega_p\Omega_{s0}(t)\mathrm{Im}[\rho_{12}],$$

$$\frac{\partial \Omega_{s0}}{\partial t} = c\frac{\partial \Omega_{s0}}{\partial z} = \frac{\eta}{2(\Delta_s + \alpha_s t)}\kappa_{23}\omega_s\Omega_{p0}(t)\mathrm{Im}[\rho_{12}],$$

$$\frac{\partial \Omega_{pr0}}{\partial t} = c\frac{\partial \Omega_{pr0}}{\partial z} = \frac{\eta}{2(\Delta_{as} + \alpha_{pr}t)}\kappa_{24}\omega_{pr}\Omega_{as0}(t)\mathrm{Im}[\rho_{12}],$$

$$\frac{\partial \Omega_{as0}}{\partial t} = c\frac{\partial \Omega_{as0}}{\partial z} = -\frac{\eta}{2(\Delta_{as})}\kappa_{14}\omega_{as}\Omega_{pr0}(t)\text{Im}[\rho_{12}].$$
(A19)

## APPENDIX B: THE STRUCTURE OF THE DEEP NEURAL NETWORKS

Both the classification and the regression neural networks share the same core structure. Since the numerical pulses, which we generated as the training data, have 2500 time steps, all models have the input shape of $2500 \times 1$. There are three blocks of the miniconvolutional neural network in the models. The first block contains three one-dimensional (1D) convolutional layers with a kernel size of 3. The second block has two layers of the 1D convolutional network with a kernel size of 5. The third block has a single 1D convolutional layer with a kernel size of 7. All the convolutional layers are activated by the rectified linear unit (ReLU) function [58] and group normalization [59]. There is a maximum pooling layer of pool size 4 after each block. There is a linear layer of size 1024 after the output of the convolutional blocks is flattened.

The structure of the neural network, shown in Fig. 11, is determined by the validation results, together with the other hyperparameters, such as the learning rate, the choice of optimizer, and the regularization. We adjust the kernel size, the number of blocks, and the number of layers in each block to have the optimal validation result. The 1D convolution layers are used because they are suitable for extracting the information within the subregion of the whole input tensor. This matches our aim, which is to extract the instantaneous value of the analytical parameter from the numerical sequential, time-dependent data. Besides, we use several 1D convolution layers as a block to extract the high-dimension information from the input tensor. Three kernels of size 3 cover the same area of the input tensor as a single kernel of size 7, but the former catches higher-dimension information than the latter. We did not set all blocks to three layers of kernel size 3 because we would like to control the overfitting problem.

[1] *Coherent Raman Scattering Microscopy*, edited by J.-X. Cheng and X. S. Xie (Taylor & Francis, Boca Raton, FL, 2013).

[2] M. Dantus, R. M. Bowman, and A. H. Zewail, Femtosecond laser observations of molecular vibration and rotation, Nature (London) **343**, 737 (1990).

[3] S. A. Malinovskaya, Observation and control of molecular motion using ultrafast laser pulses, in *Trends in Chemical Physics Research*, edited by A. N. Linke (Nova Science, New York, 2005), pp. 257–280.

[4] S. A. Malinovskaya, Chirped pulse control methods for imaging of biological structure and dynamics, Int. J. Quant. Chem. **107**, 3151 (2007).

[5] S. A. Malinovskaya, Mode selective excitation using ultrafast chirped laser pulses, Phys. Rev. A **73**, 033416 (2006).

[6] H. Zhu, Y. Li, S. Vdović, S. Long, G. He, and Q. Guo, Femtosecond coherent anti-Stokes Raman scattering spectroscopy of hydrogen bonded structure in water and aqueous solutions, Spectrochim. Acta, Part A **151**, 262 (2015).

[7] M. Lindley, K. Hiramatsu, H. Nomoto, F. Shibata, T. Takeshita, S. Kawano, and K. Goda, Ultrafast simultaneous Raman-fluorescence spectroscopy, Anal. Chem. **24**, 15563 (2019).

[8] C. E. Dedic, T. R. Meyer, and J. B. Michael, Single-shot ultrafast coherent anti-Stokes Raman scattering of vibrational/rotational nonequilibrium, Optica **4**, 563 (2017).

[9] G. Matthäus, S. Demmler, M. Lebugle, F. Küster, J. Limpert, A. Tünnermann, S. Nolte, and R. Ackermann, Ultra-broadband two beam CARS using femtosecond laser pulses, Vib. Spectrosc. **85**, 128 (2016).

[10] N. V. Vitanov, A. A. Rangelov, B. W. Shore, and K. Bergmann, Stimulated Raman adiabatic passage in physics, chemistry, and beyond, Rev. Mod. Phys. **89**, 015006 (2017).

[11] A. Bahari, A. A. Zhdanova, M. Shutova, and A. V. Sokolov, Synthesis of ultrafast waveforms using coherent Raman sidebands, Phys. Rev. A **102**, 013520 (2020).

[12] G. Fumero, C. Schnedermann, G. Batignani, T. Wende, M. Liebel, G. Bassolino, C. Ferrante, S. Mukamel, P. Kukura, and T. Scopigno, Two-Dimensional Impulsively Stimulated Resonant Raman Spectroscopy of Molecular Excited States, Phys. Rev. X **10**, 011051 (2020).

[13] H. Miller, Z. Zhou, J. Shepherd, A. J. M. Wollman, and M. C. Leake, Single-molecule techniques in biophysics: A review of the progress in methods and applications, Rep. Prog. Phys. **81**, 024601 (2018).

[14] M. T. Bremer, P. J. Wrzesinski, N. Butcher, V. V. Lozovoy, and M. Dantus, Highly selective standoff detection and imaging of trace chemicals in a complex background using single-beam coherent anti-Stokes Raman scattering, Appl. Phys. Lett. **99**, 101109 (2011).

[15] N. Dudovich, D. Oron, and Y. Silberberg, Single-pulse coherently controlled nonlinear Raman spectroscopy and microscopy, Nature (London) **418**, 512 (2002).

[16] P. J. Wrzesinski, H. U. Stauffer, J. B. Schmidt, S. Roy, and J. R. Gord, Single-shot thermometry and OH detection via femtosecond fully resonant electronically enhanced CARS (FREE-CARS), Opt. Lett. **41**, 2021 (2016).

[17] O. Katz, A. Natan, Y. Silberberg, and S. Rosenwaks, Standoff detection of trace amounts of solids by nonlinear Raman spectroscopy using shaped femtosecond pulses, Appl. Phys. Lett. **92**, 171116 (2008).

[18] T. Koo, S. Chan, and A. A. Berlin, Single-molecule detection of biomolecules by surface-enhanced coherent anti-Stokes Raman scattering, Opt. Lett. **30**, 1024 (2005).

[19] M. O. Scully and M. S. Zubairy, *Quantum Optics* (Cambridge University Press, Cambridge, 1997).

[20] M. O. Scully, G. W. Kattawar, R. P. Lucht, T. Opatrny, H. Pilloff, A. Rebane, A. V. Sokolov, and M. S. Zubairy, FAST CARS: Engineering a laser spectroscopic technique for rapid identification of bacterial spores, Proc. Natl. Acad. Sci. USA **99**, 10994 (2002).

[21] D. Pestov, R. K. Murawski, G. O. Ariunbold, X. Wang, M. C. Zhi, A. V. Sokolov, V. A. Sautenkov, Y. V. Rostovtsev, A. Dogariu, Y. Huang, and M. O. Scully, Optimizing the laser-

pulse configuration for coherent Raman spectroscopy, Science **316**, 265 (2007).

[22] C. H. R. Ooi, G. Beadie, G. Kattawar, J. F. Reinjes, Y. Rostovtsev, M. S. Zubairy, and M. O. Scully, Theory of femtosecond coherent anti-Stokes Raman backscattering enhanced by quantum coherence for standoff detection of bacterial spores, Phys. Rev. A **72**, 023807 (2005).

[23] D. Oron, N. Dudovich, D. Yelin, and Y. Silberberg, Narrow-Band Coherent Anti-Stokes Raman Signals from Broad-Band Pulses, Phys. Rev. Lett. **88**, 063004 (2002).

[24] D. Oron, N. Dudovich, and Y. Silberberg, Femtosecond Phase-and-Polarization Control for Background-Free Coherent Anti-Stokes Raman Spectroscopy, Phys. Rev. Lett. **90**, 213902 (2003).

[25] V. V. Lozovoy, B. W. Xu, J. C. Shane, and M. Dantus, Selective nonlinear optical excitation with pulses shaped by pseudorandom Galois fields, Phys. Rev. A **74**, 041805(R) (2006).

[26] H. Li, D. A. Harris, B. Xu, P. J. Wrzesinski, V. V. Lozovoy, and M. Dantus, Coherent mode-selective Raman excitation towards standoff detection, Opt. Express **16**, 5499 (2008).

[27] S. R. Oh, J. H. Park, K. Kim, J. Y. Lee, and S. Kim, Multiplex CARS imaging with spectral notch shaped laser pulses delivered by optical fibers, Opt. Express **25**, 32178 (2017).

[28] D. R. Richardson, H. U. Stauffer, S. Roy, and J. R. Gord, Comparison of chirped-probe-pulse and hybrid femtosecond/picosecond coherent anti-Stokes Raman scattering for combustion thermometry, Appl. Opt. **56**, E37 (2017).

[29] A. Konar, V. V. Lozovoy, and M. Dantus, Stimulated emission enhancement using shaped pulses, J. Phys. Chem. A **120**, 2002 (2016).

[30] D. Pestov, X. Wang, R. K. Murawski, G. O. Ariunbold, V. A. Sautenkov, and A. V. Sokolov, Pulse shaping for mode-selective ultrafast coherent Raman spectroscopy of highly scattering solids, J. Opt. Soc. Am. B **25**, 768 (2008).

[31] A. M. D. Thomasen, T. Mukai, and T. Byrnes, Ultrafast coherent control of spinor Bose-Einstein condensates using stimulated Raman adiabatic passage, Phys. Rev. A **94**, 053636 (2016).

[32] T. Hellerer, A. M. K. Enejder, and A. Zumbusch, Spectral focusing: High spectral resolution spectroscopy with broad-bandwidth laser pulses, Appl. Phys. Lett. **85**, 25 (2004).

[33] R. M. Onorato, N. Muraki, K. P. Knutsen, and R. J. Saykally, Chirped coherent anti-Stokes Raman scattering as a high-spectral and spatial resolution microscopy, Opt. Lett. **32**, 2858 (2007).

[34] R. Glenn and M. Dantus, Single broadband phase-shaped pulse stimulared Raman spectroscopy for standoff trace explosive detection, J. Phys. Chem. Lett. **7**, 117 (2016).

[35] J. X. Cheng, A. Volkmer, and X. S. Xie, Theoretical and experimental characterization of coherent anti-Stokes Raman scattering microscopy, J. Opt. Soc. Am. B **19**, 1363 (2002).

[36] N. Pandya, G. Liu, F. A. Narducci, J. Chathanathil, and S. Malinovskaya, Creation of the maximum coherence via adiabatic passage in the four-wave mixing process of coherent anti-Stokes Raman scattering, Chem. Phys. Lett. **738**, 136763 (2020).

[37] M. Sukharev and A. Nitzan, Optics of exciton-plasmon nanomaterials, J. Phys.: Condens. Matter **29**, 443003 (2017).

[38] H. Fujisaki and J. E. Straub, Vibrational energy relaxation in proteins, Proc. Natl. Acad. Sci. USA **102**, 6726 (2005).

[39] S. Malinovskaya, Prevention of decoherence by two femtosecond chirped pulse trains, Opt. Lett. **33**, 2245 (2008).

[40] B. J. Berne, M. Borkovec, and J. E. Straub, Classical and modern methods in reaction rate theory, J. Phys. Chem. **92**, 3711 (1988).

[41] M. Gruebele and P. G. Wolynes, Vibrational energy flow and chemical reactions, Acc. Chem. Res. **37**, 261 (2004).

[42] B. C. Dian, A. Longarte, and T. S. Zwier, Conformational dynamics in a dipeptide after single-mode vibrational excitation, Science **296**, 2369 (2002).

[43] W. D. Gillespie and S. P. Sharma, Raman scattering measurements of vibrational relaxation in expanding nitrogen, in *Shock Waves @ Marseille II*, edited by R. Brun and L. Z. Dumitrescu (Springer, Berlin, 1995), pp. 229–234.

[44] M. Yasuhisa and K. Teizo, Vibrational energy relaxation of metalloporphyrins in a condensed phase probed by time-resolved resonance Raman spectroscopy, Bull. Chem. Soc. Jpn. **75**, 623 (2002).

[45] E. S. Manuilovich, V. A. Astapenko, and P. A. Golovinskiia, Propagation of ultrashort laser pulses in dry and humid air, Atmos. Oceanic Opt. **28**, 209 (2015).

[46] P. Sprangle, J. R. Peñano, and B. Hafizi, Propagation of intense short laser pulses in the atmosphere, Phys. Rev. E **66**, 046418 (2002).

[47] D. A. Skoog, D. M. West, F. J. Holler, and S. R. Crouch, *Analytical Chemistry: An Introduction*, Saunders Golden Sunburst Series, 7th ed. (Saunders College Publishing, Fort Worth, TX, 1999).

[48] R. Sabatini and M. Richardson, New techniques for laser beam atmospheric extinction measurements from manned and unmanned aerospace vehicles, Cent. Eur. J. Eng. **3**, 11 (2013).

[49] Y. LeCun, Y. Bengio, and G. Hinton, Deep learning, Nature (London) **521**, 436 (2015).

[50] O. Simeone, A brief introduction to machine learning for engineers, arXiv:1709.02840.

[51] D. M. Hawkins, The problem of overfitting, J. Chem. Inf. Comput. Sci. **44**, 1 (2004).

[52] D. Goswami, Laser Phase Modulation Approaches towards Ensemble Quantum Computing, Phys. Rev. Lett. **88**, 177901 (2002).

[53] G. Liu and S. A. Malinovskaya, Creation of ultracold molecules within the lifetime scale by direct implementation of an optical frequency comb, J. Mod. Opt. **65**, 1309 (2018).

[54] D. P. Kingma and J. Ba, Adam: A method for stochastic optimization, arXiv:1412.6980.

[55] R. Caruana, S. Lawrence, and C. L. Giles, Overfitting in neural nets: Backpropagation, conjugate gradient, and early stopping, in *Advances in Neural Information Processing Systems 13: Proceedings of the 2000 Conference* (MIT Press, Cambridge, MA, 2001), pp. 402–408.

[56] N. V. Vitanov, K.-A. Suominen, and B. W. Shore, Creation of coherent atomic superpositions by fractional stimulated Raman adiabatic passage, J. Phys. B: At. Mol. Opt. Phys. **32**, 4535 (1999).

[57] G. Liu, F. A. Narducci, and S. A. Malinovskaya, Limits to remote molecular detection via coherent anti-Stokes Raman spectroscopy using a maximal coherence control technique, J. Mod. Opt. **67**, 21 (2020).

[58] V. Nair and G. Hinton, Rectified linear units improve restricted Boltzmann machines, in *Proceedings of the 27th International Conference on Machine Learning, Haifa, Israel* (Omnipress, Madison, WI, 2010), pp. 807–814.

[59] K. He, X. Zhang, S. Ren, and J. Sun, Delving deep into rectifiers: Surpassing human-level performance on ImageNet classification, in *Proceedings of the 2015 IEEE International Conference on Computer Vision (ICCV)* (IEEE, Piscataway, NJ, 2015), pp. 1026–1034.